Journal of Materials Chemistry C

ROYAL SOCIETY OF CHEMISTRY

PAPER

View Article Online
View Journal | View Issue





Cite this: J. Mater. Chem. C, 2021, 9, 14808

# Comparative study on the impact of through-space charge transfer over the electroluminescence performance of delayed fluorescence molecules†

Maoxing Yu,[a] Xiangyu Zhu,[a] Jiajie Zeng,[a] Hao Liu,[a] Ruishan Huang,[a] Zeyan Zhuang,[a] Pingchuan Shen,[a] Zujin Zhao *[a] and Ben Zhong Tang*[abc]

Received 31st July 2021,
Accepted 24th September 2021

DOI: 10.1039/d1tc03564a

rsc.li/materials-c

Through-space charge transfer (TSCT) is adopted in the design of thermally activated delayed fluorescence (TADF) emitters owing to the facile separation of frontier orbitals. However, the advantages of TSCT in the creation of TADF emitters has not been fully resolved. To address this issue, we design and synthesize a series of V-shaped molecules with TSCT and linear molecules with through-bond charge transfer (TBCT), consisting of a 1,3,5-triazine acceptor, a phenoxazine or phenothiazine donor, and an *o*- or *p*-terphenyl bridge. A comparative study is conducted to demonstrate their differences in photoluminescence (PL) and electroluminescence (EL) properties. Both kinds of molecules have apparently separated frontier orbitals and prominent aggregation-induced delayed fluorescence properties. Owing to the through-space edge-to-face alignment, the V-shaped molecules with TSCT exhibit higher solid-state PL quantum yields and faster reverse intersystem crossing processes than the linear molecules with TBCT. The V-shaped molecules hold better EL performances with higher EL efficiencies and smaller efficiency roll-offs than linear molecules, regardless of whether they are in nondoped or doped organic light-emitting diodes (OLEDs). These results indicate that TSCT could be a good choice for the creation of TADF emitters, particularly for those with long conjugation molecular backbones.

## Introduction

Purely organic thermally activated delayed fluorescence (TADF) materials with the advantages of high electroluminescence (EL) efficiency and simple molecular design have been widely exploited as emitters for organic light-emitting diodes (OLEDs), and have attracted commercial attention in the fields of displays and lighting.[1] The excellent EL performance of TADF emitters is derived from their efficient utilization of non-emissive triplet excitons in the EL process based on rapid reverse intersystem crossing (RISC) from triplet to singlet states, given a small energy gap ($\Delta E_{ST}$) between the lowest energy singlet ($S_1$) and triplet ($T_1$) excited states.[2,3] The construction of TADF emitters by introducing a charge-transfer state to separate the frontier wavefunctions located at donor (D) and acceptor (A) pairs has been gradually established, where the D and A groups are regularly bridged in a twisted way with an aromatic linker or a non-conjugated σ-spacer.[4–6] Recently, fused planar polycyclic aromatic frameworks with interesting multiresonance properties have also been utilized to realize TADF.[7–9]

For conventional D–A structured TADF systems, many strategies have been studied to accelerate RISC, such as diminishing the $\Delta E_{ST}$[10] and enhancing spin–orbit coupling.[11] However, the small $\Delta E_{ST}$ that originates from the spatial separation of frontier orbitals is often companied by a weak oscillator strength and a slow radiative transition rate, resulting in a low emission efficiency of the emitter.[12] Recently, through-space charge transfer (TSCT) between spatially adjacent D and A groups has attracted increasing interest for the design

[a] State Key Laboratory of Luminescent Materials and Devices, Guangdong Provincial Key Laboratory of Luminescence from Molecular Aggregates, South China University of Technology, Guangzhou 510640, China. E-mail: mszjzhao@scut.edu.cn
[b] Shenzhen Institute of Aggregate Science and Technology, School of Science and Engineering, The Chinese University of Hong Kong, Shenzhen 518172, Guangdong, China. E-mail: tangbenz@cuhk.edu.cn
[c] Hong Kong Branch of Chinese National Engineering Research Center for Tissue Restoration & Reconstruction, The Hong Kong University of Science and Technology, Clear Water Bay, Hong Kong, China

† Electronic supplementary information (ESI) available: Materials and instruments, NMR parameters, TGA and DSC thermograms, cyclic voltammograms, fluorescence and phosphorescence spectra, EL spectra, photophysical parameters and EL parameters. CCDC 2055132. For ESI and crystallographic data in CIF or other electronic format see DOI: 10.1039/d1tc03564a

of TADF emitters.[13–31] The spatial interaction of frontier orbitals is considered to be favourable for improving the photoluminescence (PL) quantum yield ($\Phi_{PL}$) without enlarging the $\Delta E_{ST}$. Therefore, TADF emitters based on TSCT may be promising alternatives besides conventional TADF emitters with through-bond charge transfer (TBCT). To have a clear picture of the impacts of TSCT and TBCT on the PL and EL properties of the TADF emitters, a direct comparative study on both kinds of TADF emitters will be very meaningful.

In this work, we designed and synthesized four D–A molecules with linear and V-shaped conformations, using phenoxazine (PXZ) or phenothiazine (PTZ) as the D group and triazine (TRZ) as the A group. The V-shaped molecules with TSCT, *v*-PXZTRZ and *v*-PTZTRZ, which are built on an *o*-terphenyl backbone, exhibited higher $\Phi_{PL}$ values and faster RISC processes than linear molecules, *l*-PXZTRZ and *l*-PTZTRZ, which are built with a *p*-terphenyl backbone. As a consequence, *l*-PXZTRZ and *l*-PTZTRZ exhibit better EL performances than *v*-PXZTRZ and *v*-PTZTRZ, demonstrating the important role of TSCT in the design of TADF emitters.

## Results and discussion

### Synthesis and characterization

The synthetic routes for *v*-PXZTRZ, *v*-PTZTRZ, *l*-PXZTRZ and *l*-PTZTRZ are shown in Scheme S1 (ESI†) and their structures are shown in Fig. 1. All the molecules were synthesized through two-step Suzuki reactions. They were purified *via* column chromatography, and subsequent temperature-gradient vacuum sublimation. Their structures were characterized using $^{1}$H NMR, $^{13}$C NMR and high-resolution mass spectrometry (HRMS). As revealed by thermogravimetric analysis (TGA) and differential scanning calorimetry (DSC), *v*-PXZTRZ, *v*-PTZTRZ, *l*-PXZTRZ and *l*-PTZTRZ show high thermal stability with decomposition temperature ($T_d$) values of 453, 408, 447 and 451 °C, respectively; and *v*-PXZTRZ and *v*-PTZTRZ have high glass-transition temperature ($T_g$) values of 118 and 120 °C, respectively (Fig. S1, ESI†). The electrochemical performance of the molecules was examined using cyclic voltammetry. These molecules exhibit similar electrochemical behavior, with almost identical reversible oxidation and reduction profiles as well as potential peaks; in addition, the highest occupied molecular orbital (HOMO) energy levels are approximately estimated to be in the range between −4.98 and −5.01 eV and the lowest unoccupied molecular orbital (LUMO) energy levels are in the range between −2.80 and −2.88 eV (Fig. S2, ESI†).

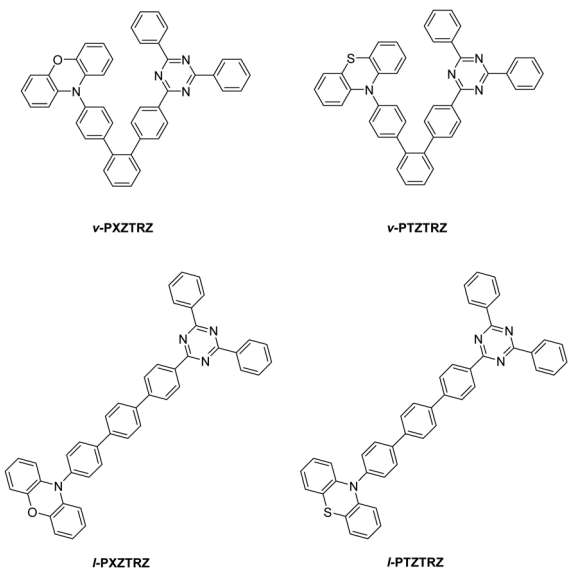


Fig. 1 Molecular structures of *v*-PXZTRZ, *v*-PTZTRZ, *l*-PXZTRZ and *l*-PTZTRZ.

### Single-crystal and electronic structures

The single crystals of *v*-PXZTRZ were obtained from a mixture of dichloromethane and ethanol by slow solvent evaporation. The crystal structure of *v*-PXZTRZ, determined *via* X-ray crystallography, shows that the central *o*-terphenyl backbone adopts a distorted V-shaped geometry with large torsion angles of 63° and 45° between the two phenyl rings (Fig. 2A). The PXZ is connected to the *o*-terphenyl backbone in a highly twisted manner, as evidenced by a large torsion angle of 82°. By contrast, the torsion angle between TRZ and the *o*-terphenyl is as small as 7°, indicative of an almost planar connection. For the whole molecule, it is worth noting that a through-space edge-to-face alignment of PXZ and TRZ is formed and the spatially separated molecular configuration can suitably reduce the electronic coupling between the electron-donating PXZ and the electron-accepting TRZ, favoring the effective separation of the HOMO and LUMO to realize a small $\Delta E_{ST}$. The visualization of such intramolecular interactions is obtained using the independent gradient model (IGM) method[32,33] on the basis of the optimized excited-state conformation (Fig. 2B and Fig. S3, ESI†), where the green sections between the two phenyl rings around the phenyl bridge as well as between PXZ (PTZ) and TRZ clearly show that a through-space interaction exists in *v*-PXZTRZ and *v*-PTZTRZ. Meanwhile, multiple weak interactions such as C–H···π and C–H···N hydrogen bonding interactions are found in the crystals, which can effectively suppress

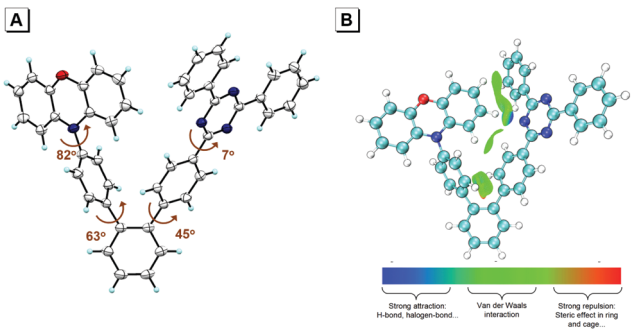


Fig. 2 (A) Single-crystal structure of *v*-PXZTRZ (CCDC 2055132). (B) Visualization of the through-space interaction of *v*-PXZTRZ, calculated based on the optimized excited-state conformation.

intramolecular motion, and thus inhibit nonradiative decay in the solid state.[34]

To study the electronic structures of these molecules, theoretical calculations based on time-dependent density functional theory (TD-DFT) simulations with M06-2X/6-31G* were performed. As illustrated in Fig. 3, for V-shaped *v*-PXZTRZ and *v*-PTZTRZ, the HOMOs are mainly distributed on PXZ and PTZ, while the LUMOs are mainly located on TRZ with partial extension to *o*-terphenyl, featuring obvious separation of the frontier orbitals. For linear *l*-PXZTRZ and *l*-PTZTRZ, their HOMOs are distributed on PXZ and PTZ, while the LUMOs are located on TRZ and the entire *p*-terphenyl. Obviously, for the V-shaped molecules, their HOMOs and LUMOs are better separated than those of the linear ones, which may lead to more efficient RISC.

## Photophysical behavior

The UV-vis absorption spectra in dilute toluene solutions of these molecules are displayed in Fig. 4A. The absorption maxima of *v*-PXZTRZ and *v*-PTZTRZ are shown at 306 and 311 nm, respectively, while *l*-PXZTRZ and *l*-PTZTRZ exhibit more red-shifted absorption maxima, at 322 and 323 nm, respectively, with a stronger absorption intensity due to better conjugation of the linear molecular backbone. The weak absorption peaks from the intramolecular charge transfer (ICT) states are hardly observed in both linear and V-shaped molecules. In toluene solutions, *v*-PXZTRZ emits mainly at 528 nm, while *v*-PTZTRZ emits at 430 and 540 nm (Fig. S4, ESI†). In toluene, *l*-PXZTRZ and *l*-PTZTRZ both show blue-shifted PL peaks at ~490 nm due to the weaker ICT because of the long distance between the D and A groups; *l*-PTZTRZ also shows dual emission with another PL peak at 440 nm. To further explore the mechanism of dual emission, the potential energy surfaces of all the molecules in their ground states under vacuum are explored (Fig. S5, ESI†). It is found that all the molecules have their most stable conformation in a quasi-equatorial alignment with large torsion angles between the donors and the adjacent benzenes. Differently, the molecules *v*-PTZTRZ and *l*-PTZTRZ can have additional high-energy metastable quasi-axial conformers, accounting for the short-wavelength emissions in toluene solutions. Owing to the more twisted structure, *v*-PXZTRZ shows a smaller $\Phi_{PL}$ of 23.9% than that of *l*-PXZTRZ (32.1%). The same trend can also be observed

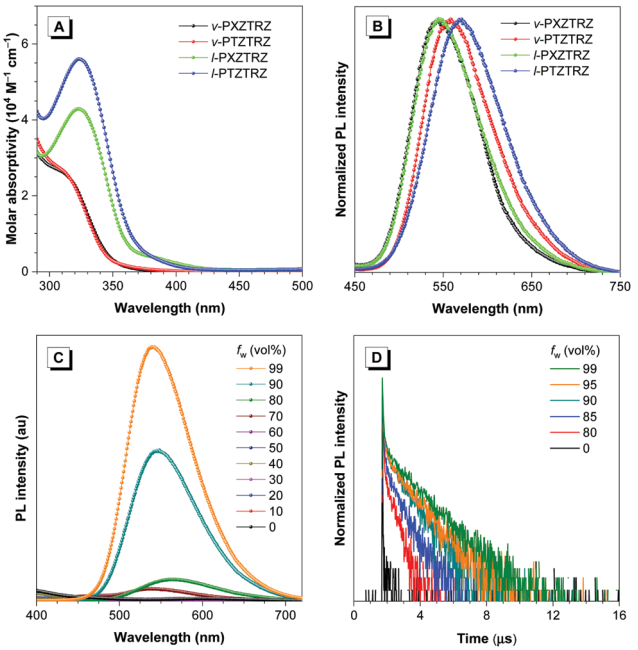


Fig. 4 (A) Absorption spectra in toluene solutions ($10^{-5}$ M) and (B) PL spectra in neat films. (C) PL spectra and (D) transient PL decay spectra of *v*-PXZTRZ in THF/water mixtures with different water fraction ($f_w$) values.

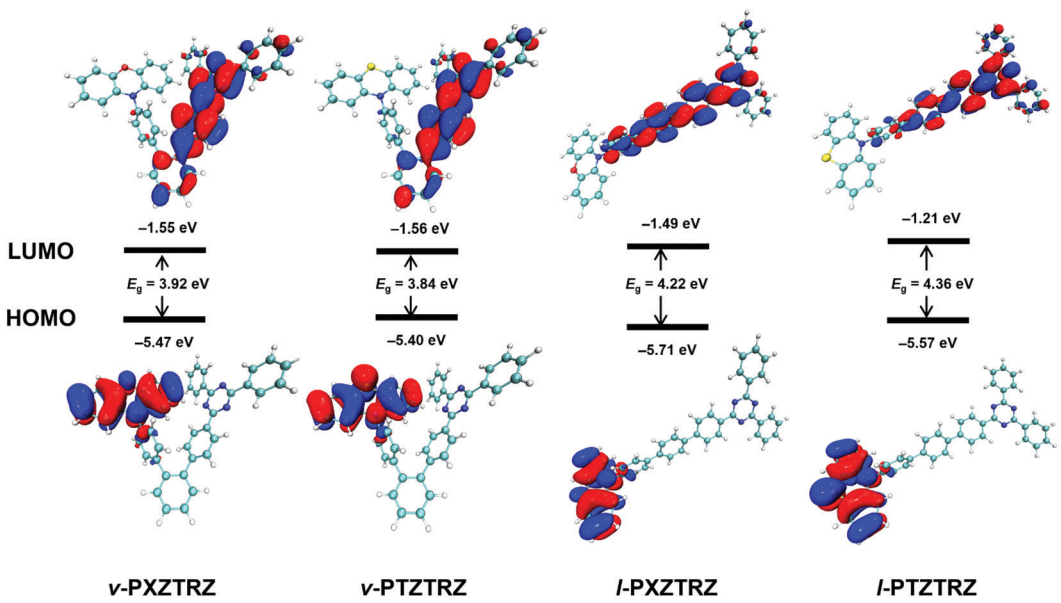


Fig. 3 Spatial distributions of HOMOs and LUMOs of the new molecules, calculated using M06-2X at the basis set level of 6-31G*.

 

Table 1 Photophysical properties of *v*-PXZTRZ, *v*-PTZTRZ, *l*-PXZTRZ and *l*-PTZTRZ

| | Soln[a] | | | | Neat film[b] | | | | | | | |
|---|---|---|---|---|---|---|---|---|---|---|---|---|
| | $\lambda_{abs}$ (nm) | $\lambda_{em}$ (nm) | $\Phi_{PL}$[c] (%) | $\tau$[c] (ns) | $\lambda_{em}$ (nm) | $\Phi_{PL}$[c] (%) | $\tau$[d] (μs) | $\tau_{prompt}$[e] (ns) | $\tau_{delayed}$[e] (μs) | $R_{delayed}$[f] (%) | $k_{RISC}$[g] ($\times 10^6$ $s^{-1}$) | $\Delta E_{ST}$[h] (eV) |
| *v*-PXZTRZ | 306 | 527 | 23.9 | 156.4 | 544 | 28.7 | 1.2 | 49.1 | 1.6 | 72.6 | 2.3 | 0.026 |
| *v*-PTZTRZ | 311 | 430, 538 | 6.6 | 13.4, 47.1 | 547 | 27.2 | 2.3 | 24.1 | 2.8 | 81.7 | 2.0 | 0.012 |
| *l*-PXZTRZ | 322 | 491 | 32.1 | 7.8 | 559 | 15.7 | 0.3 | 77.9 | 2.0 | 12.6 | 0.6 | 0.021 |
| *l*-PTZTRZ | 323 | 440, 490 | 12.1 | 1.6, 3.4 | 570 | 12.4 | 1.0 | 34.8 | 2.2 | 43.6 | 0.8 | 0.024 |

[a] In toluene solution ($10^{-5}$ M) at room temperature. [b] Vacuum-deposited on a quartz substrate. [c] Determined under nitrogen at room temperature. [d] Mean fluorescence lifetime evaluated at 300 K under nitrogen. [e] Fluorescence lifetimes of prompt ($\tau_{prompt}$) and delayed ($\tau_{delayed}$) components evaluated at 300 K under nitrogen. [f] Ratio of delayed component. [g] Rate constant of RISC calculated from the equations given in ESI. [h] Estimated from the high-energy onsets of fluorescence and phosphorescence spectra at 77 K.

between *v*-PTZTRZ and *l*-PTZTRZ (Table 1). On the other hand, the $\Phi_{PL}$ values of PTZ-substituted *v*-PTZTRZ and *l*-PTZTRZ are smaller than those of PXZ-substituted *v*-PXZTRZ and *l*-PXZTRZ, which can be attributed to the energy loss from the transformation between quasi-axial and quasi-equatorial conformers.

However, in neat films, the PL peaks of *v*-PXZTRZ (544 nm) and *v*-PTZTRZ (547 nm) are bluer than those of *l*-PXZTRZ (559 nm) and *l*-PTZTRZ (570 nm); and the $\Phi_{PL}$ values of *v*-PXZTRZ (28.7%) and *v*-PTZTRZ (27.2%) are higher than those of *l*-PXZTRZ (15.7%) and *l*-PTZTRZ (12.4%). The bluer emissions and higher $\Phi_{PL}$ values of the V-shaped molecules are relevant to the relatively weaker intermolecular interactions in neat films due to their highly twisted molecular structures. Moreover, different from the solution state, *v*-PTZTRZ and *l*-PTZTRZ in neat films show no short-wavelength emissions (Fig. 4B), because the molecules adopt more stable quasi-equatorial conformations, and the conformational change is suppressed by spatial constraints.

To further explore their photophysical characteristics, the PL spectra in tetrahydrofuran (THF)/water mixtures with different proportions were measured (Fig. 4C and Fig. S6, ESI†). For *v*-PXZTRZ, the PL intensity decreases in low water fraction ($f_w$) mixtures, and then increases sharply along with the increase in $f_w$, which can be attributed to competition between the ICT effect and restriction of intramolecular motion.[35] When water is added to THF at low $f_w$, the increased polarity of the mixed solution strengthens the ICT effect, and thus leads to a decreased PL intensity. With the increase of $f_w$, the formation of aggregates activates the restriction of intramolecular motion, and thus suppresses the nonradiative process of the excited state, resulting in an enhanced PL intensity.[36]

A small singlet–triplet energy gap is favorable to realize the TADF property. To further understand the PL properties, the fluorescence and phosphorescence spectra of their neat films at 77 K were investigated (Fig. S7, ESI†), and the $\Delta E_{ST}$ values of these molecules were calculated (Table 1). Small $\Delta E_{ST}$ values of 0.026, 0.012, 0.021 and 0.024 eV were obtained for *v*-PXZTRZ, *l*-PXZTRZ, *v*-PTZTRZ and *l*-PTZTRZ, respectively, which allow a fast RISC process from $T_1$ to $S_1$ and endow the molecules with evident delayed fluorescence. Moreover, their transient PL decay spectra in toluene solutions and neat films were measured at room temperature. In toluene solution, *v*-PXZTRZ shows a mean PL lifetime of 156.4 ns, consisting of prompt fluorescence ($\tau_{prompt}$) of 91.6 ns and delayed fluorescence ($\tau_{delayed}$) of 932.1 ns (Fig. S8, ESI†). The PL lifetime of *v*-PTZTRZ is shorter than that of *v*-PXZTRZ, due to the quasi-axial and quasi-equatorial conformational change. However, the linear molecules *l*-PXZTRZ and *l*-PTZTRZ show much shorter PL lifetimes without prominent delayed fluorescence, which is attributed to the faster internal conversion (IC) in the more flexible linear molecular structures. In solid films, *v*-PXZTRZ, *v*-PTZTRZ, *l*-PXZTRZ and *l*-PTZTRZ show microsecond-scale delayed lifetimes of 1.6, 2.8, 2.0 and 2.2 μs, corresponding to the ratio the of delayed components of 72.6%, 81.7%, 12.6% and 43.6%, respectively (Table 1 and Table S1, ESI†). The V-shaped molecules, *v*-PXZTRZ and *v*-PTZTRZ, which possess the TSCT effect, have larger $k_{RISC}$ values of $2.3 \times 10^6$ and $2.0 \times 10^6$ $s^{-1}$, respectively, over those of *l*-PXZTRZ and *l*-PTZTRZ ($0.6 \times 10^6$ and $0.8 \times 10^6$ $s^{-1}$, respectively). On the other hand, the transient decay PL spectra at various temperatures were also measured (Fig. S9, ESI†) in which the enhancement of delayed fluorescence is basically correlated with the increase in temperature, further validating the TADF characteristics of these molecules. These results unquestionably demonstrate the positive effect of TSCT in the design of TADF emitters, while TBCT may become less efficient in linear TADF emitters that have long conjugated molecular backbones.

To figure out the dynamic changing tendency of the photophysical behavior in the aggregated state, the transient PL decay spectra in THF/water mixtures were measured (Fig. 4D and Fig. S10, ESI†). In THF solutions, these molecules exhibit nanoscale PL lifetimes without recognizable delayed components. By adding water to the THF solutions, prominent delayed fluorescence is observed, and the ratio of the delayed components is enhanced roughly with the increase in $f_w$, verifying the typical aggregation-induced delayed fluorescence (AIDF) characteristics (Table S2, ESI†). In THF solutions, the highly active IC process *via* intramolecular motion can deactivate the excited state and have an advantage over the competition with the ISC and RISC processes, leading to weak emission and the absence of the delayed component. However, when the molecules are aggregated in the THF/water mixtures with high $f_w$ values or in solid films, the restricted intramolecular motion can block the IC channels, and then allow the ISC and RISC processes. As a consequence, delayed fluorescence appears and strengthens upon the formation of aggregates.[37–40]

## Electroluminescence

To further study the impact of TSCT on the EL properties, nondoped OLEDs of *v*-PXZTRZ, *v*-PTZTRZ, *l*-PXZTRZ and

*l*-PTZTRZ were fabricated, with the structure of ITO/HATCN (5 nm)/TAPC (20 nm)/TCTA (5 nm)/emitter (35 nm)/TmPyPB (55 nm)/LiF (1 nm)/Al (where emitter = *v*-PXZTRZ, device I; *v*-PTZTRZ, device II; *l*-PXZTRZ, device III; and *l*-PTZTRZ, device IV) in which HATCN (dipyrazino[2,3-*f*:2′,3′-*h*]quinoxaline2,3,6,7,10,11-hexacarbonitrile) serves as the hole-injection layer; TAPC (di-(4-(*N*,*N*-ditolylamino)phenyl)cyclohexane) and TmPyPB (1,3,5-tri(*m*-pyridin-3-ylphenyl)benzene) are used as the hole- and electron-transporting layers, respectively; and 4,4′,4″-tris(carbazol-9-yl)-triphenylamine (TCTA) is adopted as the exciton blocking layer. The devices I–IV are turned on at low voltages of 2.8–3.2 V (Table 2), revealing a relatively unimpeded carrier injection and transport process in the emitters. All these devices emit yellow light with the EL peaks at 554–585 nm (Fig. 5), which are consistent with their PL peaks of neat films (Table 1). Device I of *v*-PXZTRZ gives a high EL performance with a maximum external quantum efficiency ($\eta_{ext}$), current efficiency ($\eta_C$), power efficiency ($\eta_P$), and luminance ($L$) of 9.9%, 30.9 cd $A^{-1}$, 26.5 lm $W^{-1}$ and 19013 cd $m^{-2}$, respectively. Device II of *v*-PTZTRZ shows maximum $\eta_{ext}$, $\eta_C$, $\eta_P$ and $L$ values of 8.0%, 21.1 cd $A^{-1}$, 19.2 lm $W^{-1}$ and 20854 cd $m^{-2}$, respectively (Fig. 5 and Fig. S11, ESI†). The similar photophysical properties for the V-shaped molecules give these devices a similar EL performance. However, for the linear molecules, devices III and IV fabricated based on *l*-PXZTRZ and *l*-PTZTRZ display inferior EL performances, only affording maximum $\eta_{ext}$, $\eta_C$, $\eta_P$ and $L$ of 2.4%, 6.8 cd $A^{-1}$, 5.6 lm $W^{-1}$, and 3760 cd $m^{-2}$; and 1.9%, 4.2 cd $A^{-1}$, 2.8 lm $W^{-1}$, and 3164 cd $m^{-2}$, respectively. The better EL performances of *v*-PXZTRZ and *v*-PTZTRZ should be attributed to the higher $\Phi_{PL}$ values and the faster RISC process, owing to the efficient TSCT. Moreover, device I of *v*-PXZTRZ retains a high $\eta_{ext}$ of 9.5% at 1000 cd $m^{-2}$ with a small efficiency roll-off, which can be attributed to the suppression of exciton annihilation by its highly twisted structure. These results disclose that the V-shaped molecules perform better than the linear molecules in OLEDs, furnishing better EL efficiencies and small efficiency roll-offs.

To further broaden the application of these molecules, their behaviors in doped OLEDs were investigated. Doped OLEDs with configurations of ITO/HATCN (5 nm)/TAPC (50 nm)/TCTA (5 nm)/*x* wt% emitter: TmPyPB (20 nm)/TmPyPB (40 nm)/LiF (1 nm)/Al (where emitter = *v*-PXZTRZ, *v*-PTZTRZ, *l*-PXZTRZ, and *l*-PTZTRZ; *x* = 10, 20, 30) were fabricated. As listed in Table 2, all the doped OLEDs show low turn-on voltages of 2.8–3.0 V. The doped OLEDs have shorter EL wavelengths than the nondoped OLEDs, which can be attributed to the weaker intermolecular interactions among the emitter molecules and the lowered ICT effect due to the decreased polarity of the doped film compared with that of the neat film. On the other hand, due to the greatly reduced steric hindrance, the linear molecules have much stronger intermolecular π–π stacking interactions than the V-shaped molecules in neat films. Therefore, in comparison with V-shaped molecules, the linear molecules show much larger blue-shifts from nondoped devices to doped devices. Devices V and VI of *v*-PXZTRZ and *v*-PTZTRZ with a 20 wt% doping concentration provide slightly better EL efficiencies with maximum $\eta_{ext}$, $\eta_C$ and $\eta_P$ of 12.6%/11.9%, 40.7/36.0 cd $A^{-1}$ and 45.6/40.4 lm $W^{-1}$, respectively (Fig. 5, Fig. S12 and S13, Table 2, Table S3 and S4, ESI†). Doped devices VII and VIII of *l*-PXZTRZ and *l*-PTZTRZ show enhanced EL efficiencies with maximum $\eta_{ext}$, $\eta_C$ and $\eta_P$ of 11.7%/9.0%, 34.3/25.7 cd $A^{-1}$ and 38.4/26.9 lm $W^{-1}$, respectively. However, the improvement in EL efficiencies of these doped OLEDs is accompanied by an increase of efficiency roll-off and the luminance intensity is sacrificed relative to that in the nondoped OLEDs (Fig. 5, Fig. S14 and S15, Tables S5 and S6, ESI†). From Table S1 (ESI†), it can be seen that the neat films of V-shaped molecules have faster RISC processes and shorter delayed fluorescence lifetimes than the doped films. As a consequence, the triplet excitons can be converted to singlet excitons for more efficient light emission, and triplet–triplet annihilation can be reduced at high voltages as well, accounting for the smaller efficiency roll-off values of the nondoped devices than those of the doped devices.[11,41,42]

To decipher the difference in the device efficiencies between the doped and undoped devices, *v*-PXZTRZ was selected as a model to study the carrier mobility *via* the space charge limited current (SCLC) method.[43] Hole- and electron-only devices with configurations of ITO/TAPC (10 nm)/emitter (80 nm)/TAPC (10 nm)/Al (where emitter = *v*-PXZTRZ and 20 wt% *v*-PXZTRZ : TmPyPB for hole-only devices H1 and H2, respectively) and ITO/TmPyPB (10 nm)/emitter (80 nm)/TmPyPB (10 nm)/LiF (1 nm)/Al (where emitter = *v*-PXZTRZ and 20 wt% *v*-PXZTRZ : TmPyPB for electron-only devices E1 and E2,

Table 2 EL performances of the nondoped and doped OLEDs[a]

| | Maximum values | | | | | Values at 1000 cd $m^{-2}$ | | | | | | |
|---|---|---|---|---|---|---|---|---|---|---|---|---|
| Device | $V_{on}$ (V) | $\eta_C$ (cd $A^{-1}$) | $\eta_P$ (lm $W^{-1}$) | $\eta_{ext}$ (%) | $L$ (cd $m^{-2}$) | $V$ (V) | $\eta_C$ (cd $A^{-1}$) | $\eta_P$ (lm $W^{-1}$) | $\eta_{ext}$ (%) | CIE ($x$,$y$) | $\lambda_{EL}$ (nm) | RO (%) |
| I: *v*-PXZTRZ | 3.1 | 30.9 | 26.5 | 9.9 | 19013 | 4.6 | 29.7 | 20.3 | 9.5 | (0.43,0.55) | 554 | 3.9 |
| II: *v*-PTZTRZ | 2.8 | 21.1 | 19.2 | 8.0 | 20854 | 4.6 | 20.4 | 13.9 | 7.8 | (0.49,0.50) | 573 | 2.5 |
| III: *l*-PXZTRZ | 3.2 | 6.8 | 5.6 | 2.4 | 3760 | 6.2 | 4.7 | 2.4 | 1.7 | (0.45,0.52) | 563 | 29.1 |
| IV: *l*-PTZTRZ | 3.2 | 4.2 | 2.8 | 1.9 | 3164 | 6.8 | 3.0 | 1.4 | 1.4 | (0.52,0.47) | 585 | 26.3 |
| V: 20 wt% *v*-PXZTRZ | 2.8 | 40.7 | 45.6 | 12.6 | 11385 | 4.0 | 33.8 | 26.5 | 10.5 | (0.40,0.56) | 550 | 16.7 |
| VI: 20 wt% *v*-PTZTRZ | 2.8 | 36.0 | 40.4 | 11.9 | 4658 | 4.6 | 10.6 | 7.2 | 3.5 | (0.42,0.54) | 556 | 70.6 |
| VII: 20 wt% *l*-PXZTRZ | 2.8 | 34.3 | 38.4 | 11.7 | 3979 | 5.8 | 4.2 | 2.3 | 1.4 | (0.31,0.51) | 532 | 88.0 |
| VIII: 10 wt% *l*-PTZTRZ | 3.0 | 25.7 | 26.9 | 9.0 | 2655 | 6.6 | 1.8 | 0.88 | 0.64 | (0.36,0.49) | 554 | 92.9 |

[a] Abbreviations: $V_{on}$ = turn-on voltage at 1 cd $m^{-2}$; $\eta_c$ = current efficiency; $\eta_p$ = power efficiency; $\eta_{ext}$ = external quantum efficiency; CIE = Commission Internationale de l'Eclairage coordinates; $\lambda_{EL}$ = EL maximum; RO = current efficiency roll-off.

 

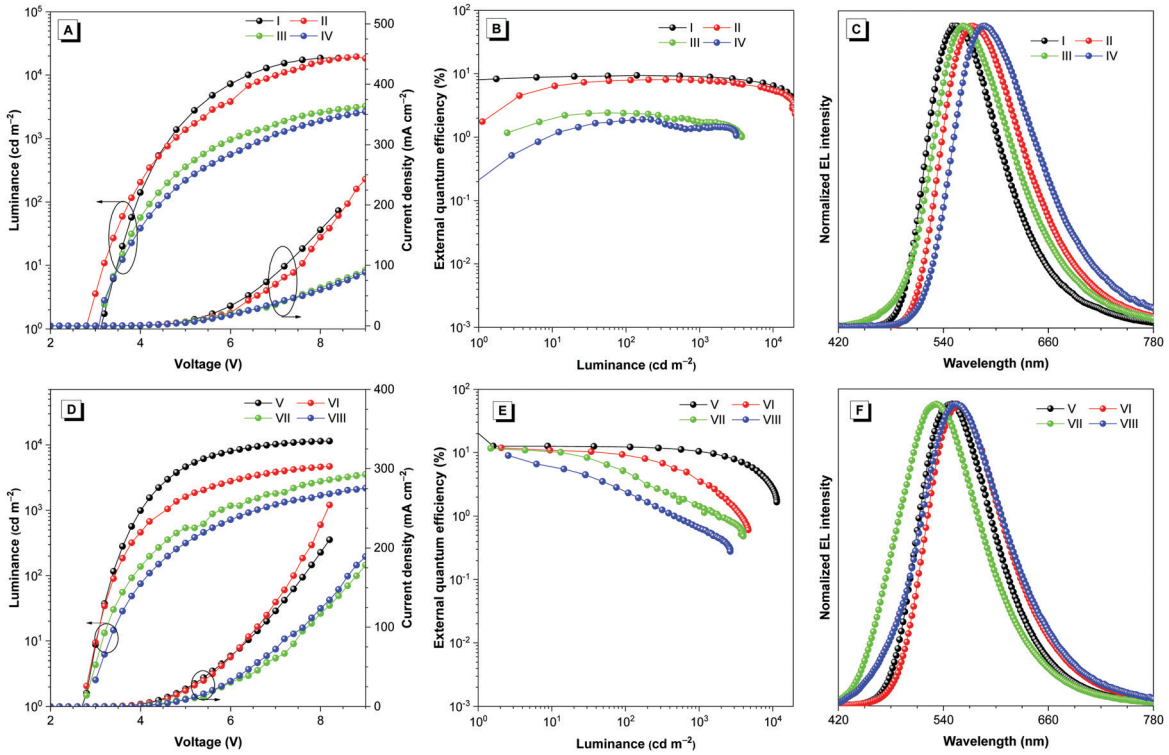


Fig. 5 Plots of (A) luminance–voltage–current density, (B) external quantum efficiency–luminance and (C) EL spectra at 1000 cd m$^{-2}$ of the nondoped OLEDs I, II, III and IV based on *v*-PXZTRZ, *v*-PTZTRZ, *l*-PXZTRZ and *l*-PTZTRZ, respectively; (D) luminance–voltage–current density, (E) external quantum efficiency–luminance and (F) EL spectra at 1000 cd m$^{-2}$ of the doped OLED devices V, VI, VII and VIII based on *v*-PXZTRZ, *v*-PTZTRZ, *l*-PXZTRZ and *l*-PTZTRZ, respectively.

respectively) were fabricated (Fig. S16, ESI†). The results reveal that *v*-PXZTRZ holds a bipolar carrier transport ability. The carrier balance in nondoped devices is slightly better than in doped devices, which can exert a positive effect over the device efficiency to some degree.

## Conclusions

In summary, a comparative study is conducted to evaluate the influence of TSCT on the delayed fluorescence. A series of V-shaped and linear D–A molecules is designed and synthesized based on *o*-terphenyl and *p*-terphenyl backbones. In comparison with linear molecules, the V-shaped molecules, in which the D groups of PXZ and PTZ and the A group of TRZ are spatially close, have a faster RISC process and higher $\Phi_{PL}$ values in neat films due to efficient TSCT, in favor of enhanced exciton utilization in OLEDs. In addition, the V-shaped molecules show the obvious AIDF effect, and can more efficiently suppress emission quenching and exciton annihilation, due to the long intermolecular distances between highly twisted molecules. The nondoped OLEDs fabricated using V-shaped molecules exhibit higher EL efficiencies of 30.9 cd A$^{-1}$, 26.5 lm W$^{-1}$ and 9.9% and a smaller efficiency roll-off of 3.9% at 1000 cd m$^{-2}$ compared with those of linear molecules. The EL performance of the doped OLED of *v*-PXZTRZ is further improved to 40.7 cd A$^{-1}$ and 45.6 lm W$^{-1}$ and 12.6% with a smaller efficiency roll-off compared with those of linear molecules. These results suggest that the introduction of TSCT could be more effective than that of linear TBCT in the creation of efficient TADF emitters, particularly for molecules with long conjugation backbones, leading to a better EL performance.

## Conflicts of interest

The authors declare no competing financial interest.

## Acknowledgements

This study was financially supported by the National Natural Science Foundation of China (21788102), the Natural Science Foundation of Guangdong Province (2019B030301003), the Innovation and Technology Commission (ITC-CNERC14SC01) and the Fundamental Research Funds for the Central Universities.

## References

1 Y. Liu, C. Li, Z. Ren, S. Yan and M. R. Bryce, *Nat. Rev. Mater.*, 2018, **3**, 18020.
2 K. Goushi, K. Yoshida, K. Sato and C. Adachi, *Nat. Photon.*, 2012, **6**, 253.

3 C. Y. Chan, M. Tanaka, H. Nakanotani and C. Adachi, *Nat. Commun.*, 2018, **9**, 5036.
4 H. Liu, J. Zeng, J. Guo, H. Nie, Z. Zhao and B. Z. Tang, *Angew. Chem., Int. Ed.*, 2018, **57**, 9290.
5 Y. Geng, A. D'Aleo, K. Inada, L.-S. Cui, J. U. Kim, H. Nakanotani and C. Adachi, *Angew. Chem., Int. Ed.*, 2017, **56**, 16536.
6 Z. Yang, Y. Zhan, Z. Qiu, J. Zeng, J. Guo, S. Hu, Z. Zhao, X. Li, S. Ji, Y. Huo and S.-J. Su, *ACS Appl. Mater. Interfaces*, 2020, **12**, 29528.
7 X. Liang, Z.-P. Yan, H.-B. Han, Z.-G. Wu, Y.-X. Zheng, H. Meng, J.-L. Zuo and W. Huang, *Angew. Chem., Int. Ed.*, 2018, **57**, 11316.
8 T. Huang, W. Jiang and L. Duan, *J. Mater. Chem. C*, 2018, **6**, 5577.
9 A. Pershin, D. Hall, V. Lemaur, J.-C. Sancho-Garcia, L. Muccioli, E. Zysman-Colman, D. Beljonne and Y. Olivier, *Nat. Commun.*, 2019, **10**, 597.
10 X. Cai and S.-J. Su, *Adv. Funct. Mater.*, 2018, **28**, 1802558.
11 J. Xu, X. Zhu, J. Guo, J. Fan, J. Zeng, S. Chen, Z. Zhao and B. Z. Tang, *ACS Mater. Lett.*, 2019, **1**, 613.
12 M. Godumala, S. Choi, M. J. Cho and D. H. Choi, *J. Mater. Chem. C*, 2019, **7**, 2172.
13 X. Zheng, R. Huang, C. Zhong, G. Xie, W. Ning, M. Huang, F. Ni, F. B. Dias and C. Yang, *Adv. Sci.*, 2020, **7**, 1902087.
14 S. Y. Yang, Q.-S. Tian, Y. J. Yu, S.-N. Zou, H.-C. Li, A. Khan, Q.-H. Wu, Z.-Q. Jiang and L.-S. Liao, *J. Org. Chem.*, 2020, **85**, 10628.
15 X. Tang, L.-S. Cui, H.-C. Li, A. J. Gillett, F. Auras, Y.-K. Qu, C. Zhong, S. T. E. Jones, Z.-Q. Jiang, R. H. Friend and L.-S. Liao, *Nat. Mater.*, 2020, **19**, 1332.
16 X. Lv, Y. Wang, N. Li, X. Cao, G. Xie, H. Huang, C. Zhong, L. Wang and C. Yang, *Chem. Eng. J.*, 2020, **402**, 126173.
17 K. Li, Y. Zhu, B. Yao, Y. Chen, H. Deng, Q. Zhang, H. Zhan, Z. Xie and Y. Cheng, *Chem. Commun.*, 2020, **56**, 5957.
18 A. Khan, Y.-K. Wang, C.-C. Huang, S. Kumar, M.-K. Fung, Z.-Q. Jiang and L.-S. Liao, *Org. Electron.*, 2020, **77**, 105520.
19 X. Cao, Z. Chen, S. Gong, K. Pan, C. Zhou, T. Huang, D. Chai, Q. Zhan, N. Li, Y. Zou, H. Liu and C. Yang, *Chem. Eng. J.*, 2020, **399**, 125648.
20 P. Zhang, J. Zeng, J. Guo, S. Zhen, B. Xiao, Z. Wang, Z. Zhao and B. Z. Tang, *Front. Chem.*, 2019, **7**, 199.
21 Z. Yang, Z. Mao, C. Xu, X. Chen, J. Zhao, Z. Yang, Y. Zhang, W. Wu, S. Jiao, Y. Liu, M. P. Aldred and Z. Chi, *Chem. Sci.*, 2019, **10**, 8129.
22 Y. K. Wang, C. C. Huang, H. Ye, C. Zhong, A. Khan, S. Y. Yang, M. K. Fung, Z.-Q. Jiang, C. Adachi and L.-S. Liao, *Adv. Opt. Mater.*, 2019, **8**, 1901150.
23 L. Gan, Z. Xu, Z. Wang, B. Li, W. Li, X. Cai, K. Liu, Q. Liang and S.-J. Su, *Adv. Funct. Mater.*, 2019, **29**, 1808088.
24 M. Auffray, D. H. Kim, J. U. Kim, F. Bencheikh, D. Kreher, Q. Zhang, A. D'Aléo, J. C. Ribierre, F. Mathevet and C. Adachi, *Chem. – Asian J.*, 2019, **14**, 1921.
25 E. Spuling, N. Sharma, I. D. W. Samuel, E. Zysman-Colman and S. Bräse, *Chem. Commun.*, 2018, **54**, 9278.
26 S. Shao, J. Hu, X. Wang, L. Wang, X. Jing and F. Wang, *J. Am. Chem. Soc.*, 2017, **139**, 17739.
27 H. Tsujimoto, D.-G. Ha, G. Markopoulos, H. S. Chae, M. A. Baldo and T. M. Swager, *J. Am. Chem. Soc.*, 2017, **139**, 4894.
28 S. Shao and L. Wang, *Aggregate*, 2020, **1**, 45.
29 J. Yang, M. Fang and Z. Li, *Aggregate*, 2020, **1**, 6.
30 H. Yang, Q. Liang, C. Han, J. Zhang and H. Xu, *Adv. Mater.*, 2017, **29**, 1700553.
31 F. Gao, R. Du, C. Han, J. Zhang, Y. Wei, G. Lu and H. Xu, *Chem. Sci.*, 2019, **10**, 5556.
32 T. Lu and F. Chen, *J. Comput. Chem.*, 2012, **33**, 580.
33 C. Lefebvre, G. Rubez, K. Khartabil, J.-C. Boisson, J. Contreras-Garcia and E. Hénon, *Phys. Chem. Chem. Phys.*, 2017, **19**, 17928.
34 J. Mei, N. L. C. Leung, R. T. K. Kwok, J. W. Y. Lam and B. Z. Tang, *Chem. Rev.*, 2015, **115**, 11718.
35 J. Zeng, J. Guo, H. Liu, J. W. Y. Lam, Z. Zhao, S. Chen and B. Z. Tang, *Chem. – Asian J.*, 2019, **14**, 828.
36 P. Shen, Z. Zhuang, Z. Zhao and B. Z. Tang, *J. Mater. Chem. C*, 2018, **6**, 11835.
37 J. Guo, J. Fan, L. Lin, J. Zeng, H. Liu, C.-K. Wang, Z. Zhao and B. Z. Tang, *Adv. Sci.*, 2019, **6**, 1801629.
38 J. Huang, H. Nie, J. Zeng, Z. Zhuang, S. Gan, Y. Cai, J. Guo, S.-J. Su, Z. Zhao and B. Z. Tang, *Angew. Chem., Int. Ed.*, 2017, **56**, 12971.
39 J. Chen, J. Zeng, X. Zhu, J. Guo, Z. Zhao and B. Z. Tang, *CCS Chem.*, 2021, **3**, 230.
40 H. Liu, H. Liu, J. Fan, J. Guo, J. Zeng, F. Qiu, Z. Zhao and B. Z. Tang, *Adv. Opt. Mater.*, 2020, **8**, 2001027.
41 J. Guo, X.-L. Li, H. Nie, W. Luo, S. Gan, S. Hu, R. Hu, A. Qin, Z. Zhao, S.-J. Su and B. Z. Tang, *Adv. Funct. Mater.*, 2017, **27**, 1606458.
42 J. Guo, X.-L. Li, H. Nie, W. Luo, R. Hu, A. Qin, Z. Zhao, S.-J. Su and B. Z. Tang, *Chem. Mater.*, 2017, **29**, 3623.
43 J. Zeng, J. Guo, H. Liu, Z. Zhao and B. Z. Tang, *Adv. Funct. Mater.*, 2020, **30**, 2000019.

 